Enhanced radiative heat transfer via propagating surface modes in a dielectric nanowire

Jian-You Wang, Yong Zhang,* Cheng-Long Zhou, Yong Shuai, and Hong-Liang Yi
School of Energy Science and Engineering, Harbin Institute of Technology, 92, West Dazhi Street, Harbin 150001, People's Republic of China and Key Laboratory of Aerospace Thermophysics, Ministry of Industry and Information Technology, Harbin 150001, People's Republic of China

(Received 8 November 2023; revised 25 January 2024; accepted 29 January 2024; published 21 February 2024)

The photon-mediated radiative heat transfer (RHT) in the near-field regime decays dramatically with the increase of the separation distance. It is an open problem in applied physics to realize super-Planckian transport behaviors over long distances. This work aims to theoretically explore RHT in a many-body system consisting of nanoparticles (NPs) and a dielectric nanowire (NW). The results show that the coupling effect of localized surface phonon polaritons (SPhPs) with propagating surface modes can enhance the RHT between two interacting NPs. The maximum enhancement ratio in the presence of a NW can reach up to five orders of magnitude, higher than that of the thin film and semi-infinite slab under the same conditions. In addition, we construct a dual waveguide system consisting of a one-dimensional linear NP array and a NW. Due to the synergistic effect between the strong interactions of localized SPhPs and the propagating surface modes along the NW, the dual waveguide mode can compensate for the decrease in RHT due to the increase in spacing, thus achieving ultrastrong, long-range energy transport between NPs at both ends. The present work has potential applications in the contactless energy conversion and management of optoelectronic devices at the micro- and nanoscale.

DOI: 10.1103/PhysRevB.109.075423

I. INTRODUCTION

As a contactless energy transport mechanism, radiative heat transfer (RHT) mediated by photons has been playing a crucial role in all scales of physics from microscopic to macroscopic [1–3]. When the distance between two objects is smaller than the characteristic thermal wavelength, RHT occurs in the near-field regime where Planck's law no longer applies [4–6]. Since the excitation of evanescent electromagnetic modes, such as surface plasmon polaritons (SPPs) and surface phonon polaritons (SPhPs), near-field radiative heat transfer (NFRHT) can be improved by several orders of magnitude beyond the blackbody limit predicted by Planck's law [7–12]. Moreover, due to the rapid development of micro- and nanoscale heat transfer and the urgent need for optical devices, a great deal of attention has been recently paid to NFRHT, which offers potential prospects for efficient utilization of energy at mesoscopic scales [13–16]. However, the near-field effect decays exponentially with the increase of vertical distance from the emitting surface, which severely limits the long-distance energy transport between objects [17]. Therefore, how to realize super-Planckian transport behavior over long distances is an intriguing problem, which is of great significance for the realization of high-performance thermal management devices.

It is well known that, due to the evanescent waves playing no role in the thermal radiation of an isolated object, the near-field effect can only occur in systems including two or more objects [1]. The problems of two-body systems on NFRHT are mainly carried out in the rigorous framework of fluctuational electrodynamics (FE), involving structures such as spheres, cylinders, and slabs [18–22]. Since many-body radiative heat transfer theory was proposed [23], many scholars have investigated the novel physical phenomena and transport behaviors arising from the strong coupling of evanescent modes in complex many-body systems [24]. It is found from the literature that a lot of works have explored structures such as a semi-infinite slab [25–27], single or multilayer thin film [28–32], sphere [33], and metasurface [34–36] to enhance or regulate the photon-mediated transport behaviors, and these works are of great significance for the studies of NFRHT caused by many-body interactions.

In addition, the literature review indicates that cylindrical nanowires with outstanding optical properties have received considerable attention in NFRHT and Casimir forces [19–21,37–40], but are less frequently reported in related studies on energy transport mediated by propagating surface modes. Recently, it has been reported that a perfectly conducting cylinder can transfer energy in the form of surface waves over arbitrarily long distances with almost no loss [41], and their works provide a different concept for enhancing RHT between objects via surface modes. In this work, we employ a dielectric nanowire (NW) to enhance photon-mediated energy transfer in many-body systems. The effects of NW, thin film, and semi-infinite slab on RHT between two nanoparticles (NPs) are investigated by Green's function method, respectively. Subsequently, we propose a dual waveguide system consisting of a one-dimensional linear NP array and a NW, which can provide a reliable strategy for achieving ultrastrong, long-range energy transport between arbitrary objects. The structure of this paper is as follows: In Sec. II, the

*Corresponding author: yong_zhang@hit.edu.cn

 ©2024 American Physical Society

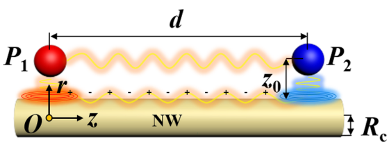

FIG. 1. The schematic of RHT between NPs via propagating surface modes in a dielectric NW.

mathematical-physical model of the entire system described by Green's function method is established, and the expression of the thermal conductance between any two NPs is given. In Sec. III, we present the main results of RHT between two NPs in the presence of different substrates. The effect of dual waveguide mode on RHT is studied. Finally, in Sec. IV, we give some conclusions and perspectives for this work.

II. THEORETICAL ASPECTS

In this work, we consider the RHT between two NPs P_1 and P_2 in the presence of a dielectric NW with a radius of R_c, as shown in Fig. 1. The two NPs with a radius of $R = 5$ nm are placed at the same distance z_0 from the top of NW, while the separation distance between them is set as d. The entire configuration is based on a cylindrical coordinate system (r, φ, z). The axis of the infinitely long NW is located on the z axis. The coordinates of the two NPs are denoted as $\mathbf{r}_1 = (R_c + z_0, 0, 0)$ and $\mathbf{r}_2 = (R_c + z_0, 0, d)$, respectively.

To investigate the properties of energy transport mediated by propagating surface modes, the RHT between two NPs in the presence of a NW is calculated in this work. To reasonably simplify the mathematical-physical model, the NPs are viewed as isotropic, linear, and nonmagnetic, and their sizes are much smaller than the thermal wavelength [26,27]. The present work is carried out in the framework of the dipole approximation, where two NPs can be described as simple radiating electrical dipoles [23,42,43]. The temperatures of NPs P_i $(i = 1, 2)$, NWs, and the vacuum environment are kept at T_i, T_c, and T_{env}, respectively. To drive the transport behavior from P_1 to P_2, it is assumed that the entire system is thermalized at a fixed temperature of T= 300 K, except P_1 is slightly heated to $T+\Delta T$, i.e., $T_1 = T+\Delta T$, $T_2 = T_s = T_{\mathrm{env}} = T$ [32,44]. It is worth noting that the cylinder here is considered as a boundary condition that can modify the heat exchange between two NPs, and the RHT between the NPs and the dielectric cylinder is not considered theoretically [27]. When temperature difference ΔT tends to zero, the RHT between P_1 and P_2 can be described by the thermal conductance h, which is expressed by the Green function (GF) as [32,45]

$$h = 2\int_0^{+\infty} \frac{d\omega}{\pi}\hbar\omega n'(\omega, T)k_0^4\chi^2 Tr[(\mathbb{M}^{-1}\mathbb{G})(\mathbb{M}^{-1}\mathbb{G})^*], \tag{1}$$

where $\hbar$ represents the reduced Planck constant, $n'(\omega, T)$ is the derivative with respect to the temperature T of the Bose-Einstein distribution $n(\omega, T) = [\exp(\hbar\omega/k_B T) - 1]^{-1}$, and k_B is the Boltzmann's constant. $k_0 = \omega/c$. $\mathbb{M} = \mathbf{I} - k_0^4\alpha_1\alpha_2\mathbb{G}\mathbb{G}^*$ represents the multiple reflections between NPs, and $\mathbb{G}$ is the GF of the entire system. Depending on the nature of NPs (dielectric or metallic), the electric polarizability can be expressed in the Clausius-Mossoti form,

$$\alpha_i^0(\omega) = 4\pi R^3\{[\varepsilon(\omega) - 1]/[\varepsilon(\omega) + 2]\}, \tag{2}$$

where $\varepsilon(\omega)$ is the electric permittivity. It has been reported in the literature that the average of GF should be used to correct the polarizability [46]. In the present work, the contribution of the scattering GF to polarizability is negligible due to the large distance z_0. Therefore, the dressed polarizability can be obtained by radiative correction as [27,47]

$$\alpha_i(\omega) = \alpha_i^0(\omega)/\{1 - i[k_0^3/(6\pi)]\alpha_i^0(\omega)\}. \tag{3}$$

The modified polarizability is expressed as

$$\chi(\omega) = \mathrm{Im}[\alpha_i(\omega)] - \frac{k_0^3}{6\pi}|\alpha_i(\omega)|^2. \tag{4}$$

In the presence of the vacuum-material interface, the total GF of the entire configuration can be written as

$$\mathbb{G} = \mathbb{G}_0 + \mathbb{G}_{\mathrm{sc}} \tag{5}$$

i.e., separated into a vacuum contribution and a scattering part. The vacuum part can be described by the free-space GF as [23]

$$\mathbb{G}_0 = \frac{\exp(ik_0 r)}{4\pi r} \times \left[\left(1 + \frac{ik_0 r - 1}{k_0^2 r^2}\right)\mathbf{I} + \frac{3 - 3ik_0 r - k_0^2 r^2}{k_0^2 r^2}\hat{\mathbf{r}} \otimes \hat{\mathbf{r}}\right] \tag{6}$$

with the unit vector $\hat{\mathbf{r}} = \mathbf{r}/r$, $\mathbf{r}$ being the vector linking the center of NPs P_1 and P_2; $r = |\mathbf{r}|$ and $\mathbf{I}$ denotes the unit dyadic tensor. The scattering contribution $\mathbb{G}_{\mathrm{sc}}$ from the vacuum-cylinder interface can be described as [38,41]

$$\mathbb{G}_{\mathrm{sc}} = \frac{i}{8\pi}\sum_{P,P'}\sum_{n=-\infty}^{\infty}(-1)^n\int_{-\infty}^{\infty} dk_z \mathbf{P}_{n,k_z}^{\mathrm{out}}(\mathbf{r})\otimes\mathbf{P}_{-n,-k_z}^{'\mathrm{out}}(\mathbf{r}')T_{n,k_z}^{PP'}, \tag{7}$$

where k_z is the z component of the wave vector in vacuum, n represents the multipole order, and P, $P' = [M, N]$ denote polarization (M for magnetic and N for electric). Based on the electromagnetic boundary conditions of three components at the vacuum-cylinder interface, the scattering matrix element $T_{n,k_z}^{PP'}$, corresponding to the scattering operator $\mathbb{T}$, depends on the radius R_c and the material properties, which can be deduced as [37,38,41,48]

$$T_{n,k_z}^{MM} = -\frac{J_n(qR_c)}{H_n(qR_c)}\frac{I_1 I_4 - K^2}{I_1 I_2 - K^2}, \tag{8}$$

$$T_{n,k_z}^{NN} = -\frac{J_n(qR_c)}{H_n(qR_c)}\frac{I_2 I_3 - K^2}{I_1 I_2 - K^2}, \tag{9}$$

$$T_{n,k_z}^{NM} = T_{n,k_z}^{MN} = \frac{2i}{\pi\sqrt{\varepsilon(\omega)}(qR_c)^2}\frac{K}{(I_1 I_2 - K^2)[H_n(qR_c)]^2}, \tag{10}$$

where J_n and H_n represent the Bessel function and the Hankel function of the first kind of n order. q_m and q are the wave vectors perpendicular to the z axis inside the NW and in vacuum, respectively, i.e., $q_m = \sqrt{\varepsilon(\omega)k_0^2 - k_z^2}$ and $q = \sqrt{k_0^2 - k_z^2}$. These intermediate variables can be represented as

$$I_1 = \frac{J_n'(q_m R_c)}{q_m R_c J_n(q_m R_c)} - \frac{1}{\varepsilon(\omega)} \frac{H_n'(qR_c)}{qR_c H_n(qR_c)}, \tag{11}$$

$$I_2 = \frac{J_n'(q_m R_c)}{q_m R_c J_n(q_m R_c)} - \frac{H_n'(qR_c)}{qR_c H_n(qR_c)}, \tag{12}$$

$$I_3 = \frac{J_n'(q_m R_c)}{q_m R_c J_n(q_m R_c)} - \frac{1}{\varepsilon(\omega)} \frac{J_n'(qR_c)}{qR_c J_n(qR_c)}, \tag{13}$$

$$I_4 = \frac{J_n'(q_m R_c)}{q_m R_c J_n(q_m R_c)} - \frac{J_n'(qR_c)}{qR_c J_n(qR_c)}, \tag{14}$$

$$K = \frac{nk_z c}{\sqrt{\varepsilon(\omega)} R_c^2 \omega}\left(\frac{1}{q_m^2} - \frac{1}{q^2}\right), \tag{15}$$

where $\mathbf{M}^{\text{out}}_{n,k_z}(\mathbf{r})$ and $\mathbf{N}^{\text{out}}_{n,k_z}(\mathbf{r})$ are the outgoing waves of cylindrical harmonics as a function of n and k_z, which can be found in Appendix A. J_n' and H_n' are the first order derivatives of J_n and H_n, respectively. In addition, for the sake of completeness of content, we also introduce the scattering Green's function for planar configurations, which can be found in Appendix B. We now have all the elements needed to carry out RHT calculations on the NPs and dielectric NW system.

III. RHT ASSISTED BY PROPAGATING SURFACE MODES

Based on the geometrical and mathematical-physical models constructed in Sec. II, this section aims to enhance RHT between NPs with the help of propagating surface modes in a NW. All material bodies are surrounded by fluctuating electromagnetic fields due to thermal and quantum fluctuations in internal current density. Radiative heat exchange between objects depends strongly on the dielectric properties of the medium [1,2]. Thus, the material properties of a NW play a critical role in the RHT between NPs. In this work, NPs and NW are made of the same material, silicon carbide (SiC), which is a typical polar dielectric material with a wide range of applications in high-power optoelectronic semiconductors. There are two main reasons for the choice of materials: (a) The calculation of the scattering Green's function of a NW consists of the integration of the wave vector k_z and the summation of the Bessel function and the Hankel function (the first kind) with respect to the order n, which involves a complicated calculation. Thanks to the existence of a single frequency-dependent resonance mode in the Reststrahlen band, the material properties of SiC can be easily characterized and the whole calculation can be simplified. (b) Several scholars have discussed the enhancement of RHT between NPs by the semi-infinite slab and the thin films of different thicknesses [27,49]. By comparing planar structures with a NW, we can robustly confirm the superiority of energy transport by a dielectric NW. The dielectric function of SiC can be described by the Drude-Lorentz model

$$\varepsilon(\omega) = \varepsilon_\infty \frac{\omega_L^2 - \omega^2 - i\Gamma\omega}{\omega_T^2 - \omega^2 - i\Gamma\omega}, \tag{16}$$

with $\varepsilon_\infty = 6.7$, $\omega_L = 1.83 \times 10^{14}$ rad s^{-1}, $\omega_T = 1.49 \times 10^{14}$ rad s^{-1}, and $\Gamma = 8.97 \times 10^{11}$ rad s^{-1}. SiC material supports the SPhPs in the range between ω_T and ω_L, i.e., the so-called Reststrahlen band, where the permittivity $\varepsilon(\omega)$ is negative [43]. According to the condition $\varepsilon(\omega)+2 = 0$, the resonance frequency of NPs ω_{np} is predicted by the electric polarizability, where $\omega_{\text{np}} = 1.756 \times 10^{14}$ rad s^{-1}. The surface resonance $\omega_{\text{m}} = 1.786 \times 10^{14}$ rad s^{-1} for a single SiC surface corresponds to the condition $\varepsilon(\omega)+1 = 0$.

A. Two NPs in the presence of a dielectric NW

The RHT between two NPs in the presence of a dielectric NW is numerically calculated. To illustrate the unique properties of the system, we also calculate the conductance in the presence of thin film and semi-infinite slab, respectively, for comparison. In addition to material properties, the separation distances d and z_0 are also important parameters affecting the RHT of NPs. The strategy we first design is to fix $z_0 = 50$ nm. The effects of interparticle distance d on the thermal conductance h for different substrates are explored, as shown in Fig. 2(a). It can be intuitively found that the h of all systems decreases with increasing d. When $d < 0.04$ μm, the conductance h produced in the presence of substrates is approximately equal to that of two isolated NPs in a vacuum. This suggests that when d is small, the interactions of localized SPhPs arising from NPs play a dominant role in heat exchanges, while the scattering contributions of substrates are almost negligible. However, as d increases, the surface effects from the vacuum-substrate interface come to the fore, leading to RHT higher than that of two NPs in vacuum. We find that the NW with a radius of $R_c = 0.1$ μm has a remarkable property for energy transport as compared to other substrate structures.

To visually show the amplification of substrates, a normalized dimensionless parameter $\Phi = h/h_0$ is defined. h_0 is the thermal conductance produced by two NPs in a vacuum. Figure 2(b) shows Φ as a function of d for different systems. It can be found that for the NW with a radius of $R_c = 0.1$ μm, the Φ produced by the two NPs first increases and then remains almost constant. The maximum enhancement ratio goes beyond five orders of magnitude, which is significantly higher than that of other systems. For the case of $R_c = 1$ μm, the Φ has the same trend and is lower than that of $R_c = 0.1$ μm at long distances. This indicates that the size of the dielectric NW also affects RHT between NPs, which is discussed in the following. Different from the NW systems, the Φ induced by the thin film with a thickness of 0.2 μm and the semi-infinite slab first increases and then decreases with the increase of d. The maximum enhancement ratio can reach up to four orders of magnitude and two orders of magnitude, respectively. It is worth noting that for comparison with the NW of $R_c = 0.1$ μm, the thickness of the thin film is selected as $\delta = 0.2$ μm. In addition, the two NW systems still maintain a high enhancement ratio when $d = 10 - 100$ μm. An interesting phenomenon is that with the increase in d, the RHT in the presence of a NW is approximately the same trend as that of two isolated NPs in vacuum. This may be attributed to the geometric properties; namely, compared with the planar structures, the axial surface waves of the NW may have a longer propagation length, which can enhance heat exchanges between NPs over long distances. Therefore, based on the above analysis, it is concluded that dielectric nanowires have

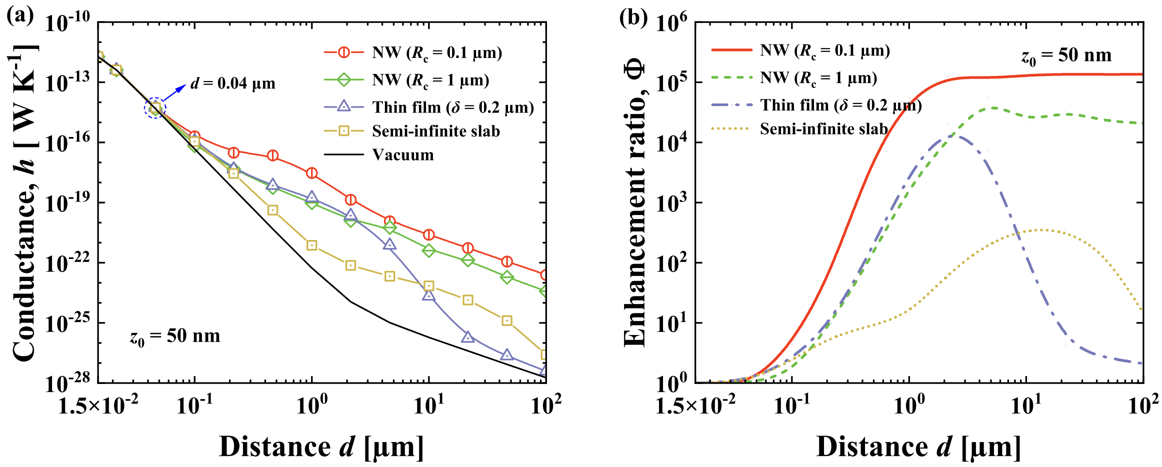

FIG. 2. (a) Thermal conductance h between two NPs in the presence of dielectric substrates as a function of d located at $z_0 = 50$ nm. (b) Enhancement ratio Φ for different systems.

superior performance in terms of enhancement of RHT as compared to planar substrates.

To gain insight into this amplification mechanism, we turn attention to the spectral analysis of RHT thermal conductance. Based on the fixed distance $z_0 = 50$ nm, the spectral conductance $h(\omega)$ between NPs is investigated for the cases of $d = 0.1$ μm and $d = 1$ μm, respectively, as shown in Fig. 3. It can be seen in Fig. 3(a) that when $d = 0.1$ μm, the $h(\omega)$ in the presence of substrates can only produce an insignificant enhancement as compared to that of two NPs in a vacuum. The coupling interactions of localized SPhPs dominate the resonance transport behaviors, and the surface effects excited by the vacuum-substrate interface make a negligible contribution at small distances. When $d = 1$ μm [see Fig. 3(b)], the increase of d weakens the coupling effect of localized SPhPs between two NPs, and the propagating surface modes arising from substrates play a critical role in RHT. Thus, the spectral conductance $h(\omega)$ in the presence of substrates is significantly higher than in a vacuum. In addition, the $h(\omega)$ of the NW with a radius of $R_c = 0.1$ μm is higher than that of other systems in the explored frequency domain, suggesting that the propagating surface waves along the NW are significant in enhancing the spectral transport intensity. It can be found that the interparticle RHT for all systems is dominated by the resonance mode, and thus, the single-frequency ω_{np} may represent the transport behaviors in the full-frequency domain.

By observing the two NW systems in Fig. 2, it is found that the radius of NW can affect the RHT between NPs. In this section, the enhancement ratio Φ as a function of R_c (or 0.5δ) and d at ω_{np} is investigated, as shown in Fig. 4. To reasonably compare the transport properties, we consider that the thickness of the thin film is equal to the diameter of NW, i.e., $\delta = 2R_c$. Compared with the thin film, the enhancement ratio of a NW goes beyond five orders of magnitude at a larger range of d; especially at a long-distance regime, the NW exhibits excellent thermal transport properties. When $d > 0.1$ μm (approximatively), the Φ produced by the two systems first increases and then decreases with the increase of R_c. Therefore, it is considered that the size effect of substrate structures has a significant impact on the RHT between NPs.

Based on the above analysis, the surface modes induced by the vacuum-substrate interface play a dominant role in achieving long-range energy transport, thus enhancing RHT between two objects. To further understand the underlying physical

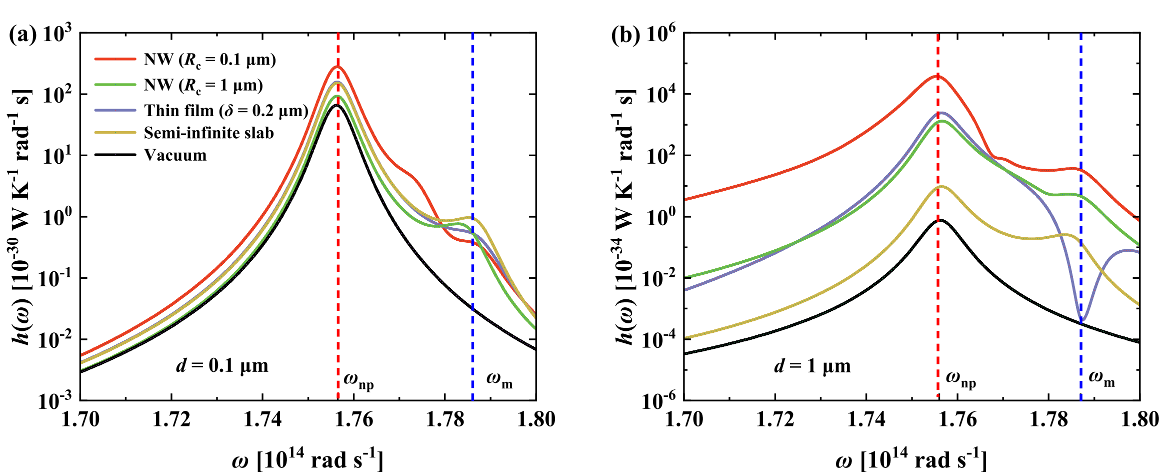

FIG. 3. Spectral analysis between two NPs located at $z_0 = 50$ nm for (a) $d = 0.1$ μm and (b) $d = 1$ μm.

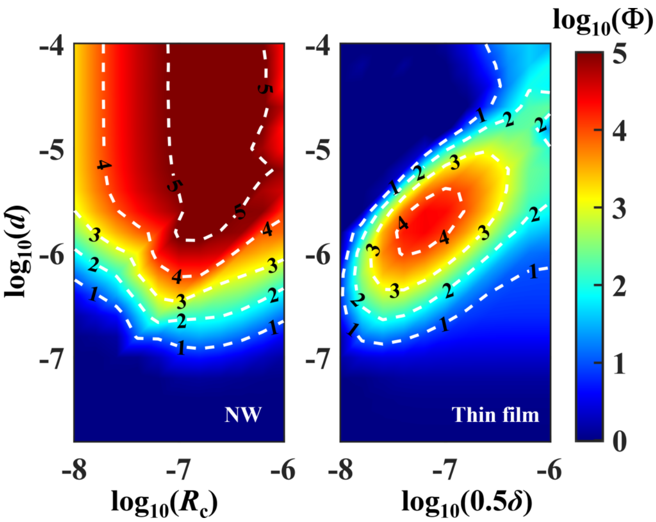

FIG. 4. Enhancement ratio Φ as a function of R_c (or 0.5δ) and d at ω_{np} for NW and thin film.

mechanisms, the traces of the scattering GF $Tr(\mathbb{G}_{sc}\mathbb{G}_{sc}^*)$ as a function of ω and k_z/β_0 for the four systems—(a) the NW of $R_c = 0.1\ \mu$m, (b) the NW of $R_c = 1\ \mu$m, (c) the thin film of $\delta = 0.2\ \mu$m, and (d) the semi-infinite slab—are shown in Fig. 5. It is noted that here that the propagation property can be characterized by the wave vector $k_z = \beta + \alpha i$ along the direction of the axis, where the real part β is the propagation constant and the imaginary part α is the attenuation constant relating to propagation loss of SPhPs. In Fig. 5, we consider that both the frequency and the wave vector are in real space, i.e., $k_z = \beta$. In addition, the wave vector k_z can be normalized by $\beta_0 = \omega_0/c$ with $\omega_0 = 10^{14}$ rad s^{-1} [29].

To gain insight into the propagation properties of energy on the vacuum-substrate interface, the dispersion relations of different systems are plotted, as shown by the grey solid line in Fig. 5. Based on the optical waveguide theory, the fundamental mode (TM$_0$ mode) is one of the best propagation modes in cylindrical waveguides, and plays a pivotal role in the propagation of electromagnetic waves in a dielectric NW [50–53]. When the order $n = 0$, by applying the boundary conditions of the electromagnetic field at $r = R_c$ on the cylindrical surface, the dispersion equation of the fundamental mode for the two structures of NW [see Figs. 5(a) and 5(b)] can be expressed as [51,54]

$$\frac{\varepsilon(\omega)}{q_m R_c}\frac{J_1(q_m R_c)}{J_0(q_m R_c)} - \frac{1}{qR_c}\frac{H_1(qR_c)}{H_0(qR_c)} = 0 \tag{17}$$

where the variables can be found in Sec. II. According to the thin film theory, the evanescent fields of the SPhPs at each interface of the thin film are able to interact with each other,

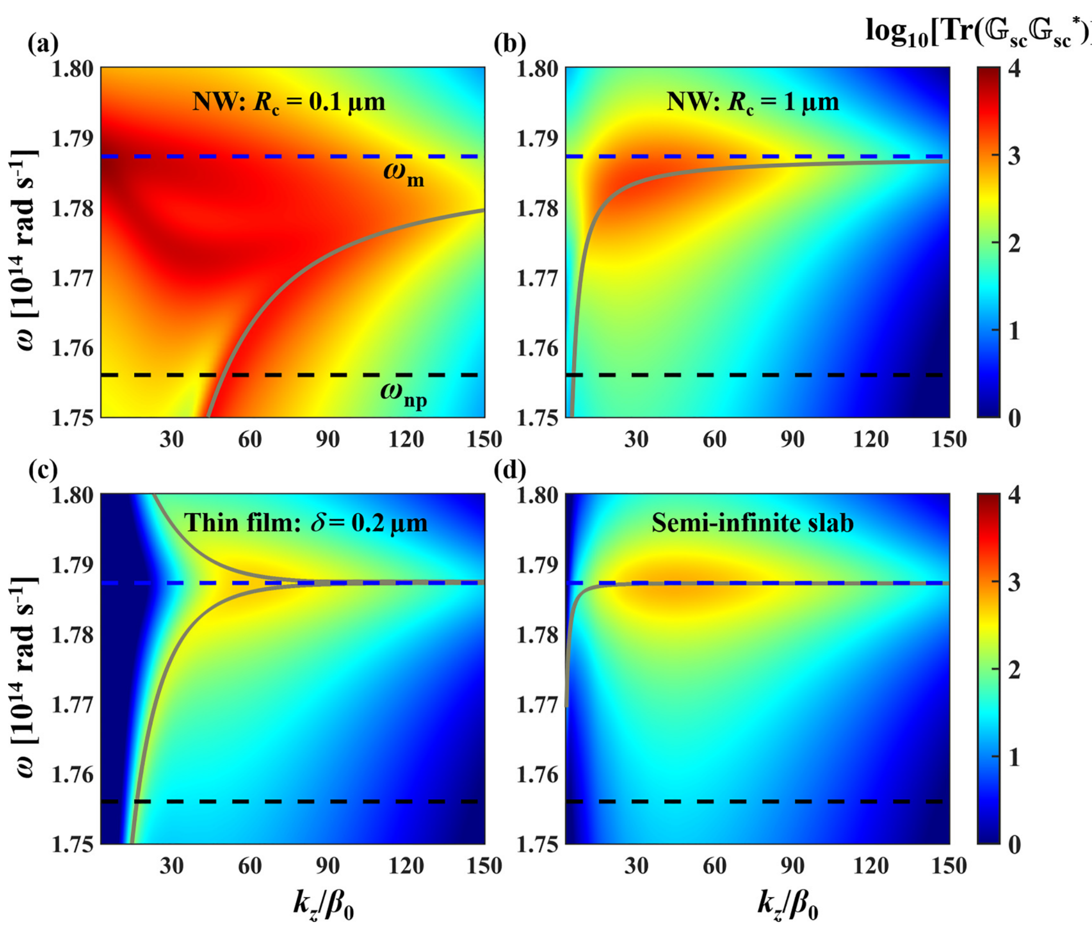

FIG. 5. $Tr(\mathbb{G}_{sc}\mathbb{G}_{sc}^*)$ as a function of ω and k_z/β_0 in the four systems at $d = 1\ \mu$m. The black dotted lines denote ω_{np}, and the blue dotted lines represent ω_m. The grey solid lines indicate the dispersion relations for different systems.

leading to the dispersion curve that splits into antisymmetric (higher frequency than $\omega_{\rm m}$) and symmetric (lower frequency than $\omega_{\rm m}$) modes. Finally, they can gradually approach the frequency $\omega_{\rm m}$ with the increase of wave vector k_z. The dispersion relation for a thin film as shown in Fig. 5(c) can be derived from the denominator of the reflection coefficient being equal to zero, which is deduced as [2]

$$\tanh(ik_{xm}\delta)\left(\frac{k_{xm}^2}{[\varepsilon(\omega)]^2}+k_x^2\right)-\frac{2k_{xm}k_x}{\varepsilon(\omega)}=0, \quad (18)$$

where the variables can be found in Appendix B. In addition, for a single semi-infinite slab, as shown in Fig. 5(d), the dispersion relation is written as [2,17]

$$K=\frac{\omega}{c}\sqrt{\frac{\varepsilon(\omega)}{\varepsilon(\omega)+1}}. \quad (19)$$

Based on the investigation of $Tr(\mathbb{G}_{\rm sc}\mathbb{G}_{\rm sc}^*)$ and the dispersion relations for different systems, it is possible to do the following analysis. First, it can be intuitively seen from Fig. 5 that compared to the other three systems, the NW with a radius of $R_{\rm c}=0.1$ µm has larger values in the explored wave vector and frequency space, which can prove that it has strong energy transport properties. In addition, by comparing Figs. 5(a) and 5(b), the wave vector k_z at the fixed frequency on the dispersion curve increases as the radius $R_{\rm c}$ decreases, and thus the transverse field distribution tends to be better localized. The performance of energy transport for the NW with a small radius may be superior. However, the propagation loss caused by the attenuation constant α increases accordingly, and the propagation length may become very small for the NW with a small radius. This leads to too much energy loss in the transport process along the NW surface. Therefore, the energy transport can first increase and then decrease with the increase of radius $R_{\rm c}$. This strongly confirms the conclusion drawn in Fig. 4, where the enhancement ratio Φ first increases and then gradually decreases as the radius increases at a long distance d. For a thin film as shown in Fig. 5(c), as the thickness decreases, the splitting of the resonance at $\omega_{\rm m}$ may become more pronounced, and the property of energy transport for the thin film may also first increase and then decrease. For a thicker film, the dispersion relation for the two modes (the antisymmetric and symmetric modes) asymptotically approximates the dispersion curve of a single semi-infinite slab [see Fig. 5(d)] with the increase of k_z/β_0. The transport behavior of thicker films gradually approaches that of the semi-infinite slab.

Based on the conclusion drawn from the spectral analysis, the single-frequency $\omega_{\rm np}$ plays a dominant role in RHT, which may represent the transport behavior in the full-frequency domain. To intuitively display the energy transport properties of different structures, the electric field energy density $u_e(\mathbf{r},\omega)$ distribution at $\omega_{\rm np}$ is calculated for the four systems when $d=0.3$ µm, as shown in Fig. 6. Here, the numerical model of $u_e(\mathbf{r},\omega)$ can be expressed as [32]

$$u_e(\mathbf{r},\omega)=\left(2\varepsilon_0^2/\pi\omega\right)\sum_j \mathrm{Im}(\alpha_j)\Theta(\omega,T_j)\mathrm{Tr}[\mathbb{Q}_{rj}\mathbb{Q}_{rj}^*], \quad (20)$$

where $\mathbb{Q}_{rj}=\omega^2\mu_0\mathbf{G}^{rj}[\mathbf{I}-\mathbf{A}]^{-1}$, and $\Theta(\omega,T_j)=\hbar\omega/\exp[(\hbar\omega/k_{\rm B}T_j)-1]$ represents the mean energy of the Planck oscillator at the temperature T_j. It can be seen that the energy density produced by the NP P_1 is much higher than around it and decays rapidly with increasing distance from P_1. Compared with the two NPs in a vacuum, the strong coupling of the localized SPhPs arising from NPs with the surface effects can enlarge the area of the high-energy density region. The substrates can produce an extra channel for energy transport from P_1 to P_2, thus enhancing the RHT between two NPs. In addition, the coupling effect between the surface modes produced by NW and the localized SPhPs is stronger than that of the thin film and semi-infinite slab, which gives P_2 a higher energy density. This suggests the NW has excellent long-range energy transport characteristics.

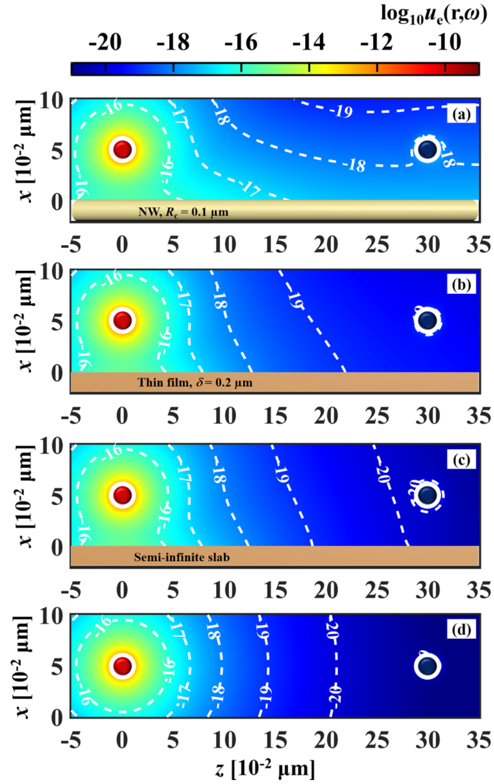

FIG. 6. The electric field energy density $u_e(\mathbf{r},\omega)$ distribution for the cases of $\omega_{\rm np}$ at $d=0.3$ µm. (a) NW with $R_{\rm c}=0.1$ µm. (b) Thin film with $\delta=0.2$ µm. (c) Semi-infinite slab. (d) Vacuum.

B. One-dimensional linear NP array above a dielectric NW

According to the conclusions drawn in the previous section, the interactions of localized SPhPs weaken with the increase in separation distance, leading to a decrease in the photon-mediated RHT between NPs. The dielectric NW can provide a channel for energy transport, thus improving heat exchange. An interesting question is whether the RHT can be further enhanced by the coupling interactions of NP arrays [55–58]. Recently, the literature has shown that anapole-based metachains are investigated experimentally, which demonstrates that the nanostructures are capable of exceeding the diffraction limit for efficient energy transport in an ultracompact manner [59]. Inspired by the ultracompact transport behaviors and the excellent properties of NWs, we further

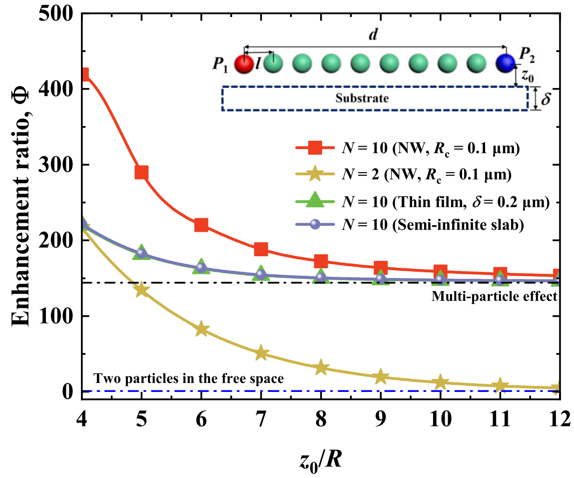

FIG. 7. The effect of z_0/R on the enhancement ratio Φ for different systems.

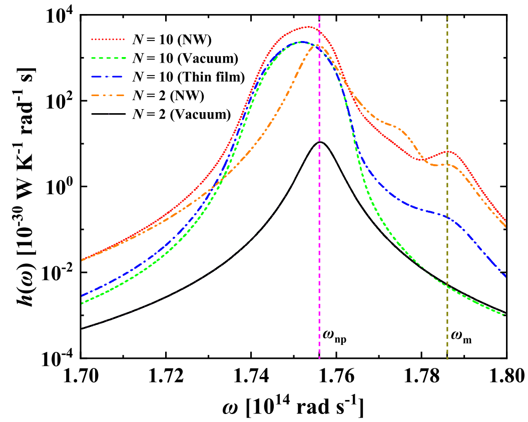

FIG. 8. Spectral analysis between two NPs located at $z_0 = 20$ nm for different systems.

investigated the effect of the interactions of a one-dimensional linear NP array and a NW on the RHT between NPs. The dual waveguide mode induced by the two structures is explored.

The configuration consisting of NP arrays and a substrate is shown in the inset in Fig. 7. The strategy we consider is that the interparticle distance is fixed at $l = 3R$, which satisfies the dipole approximation model. Without loss of generality, the distance between NPs at both ends is $d = l \times (N - 1)$, where N is the number of NP. The substrate is placed directly below the NP array, which can be a NW, thin film, or semi-infinite slab. The thickness of the substrate is set to δ, for a NW $\delta = 2R_c$, while for the semi-infinite slab, δ is nonexistent. Here, we similarly consider a NW with a radius of $R_c = 0.1$ μm and a thin film of $\delta = 0.2$ μm. By calculating the RHT between P_1 and P_2 under different systems, the coupling effects between many-particle interactions and the propagating surface modes induced by substrates are investigated.

The separation distance z_0 between the NP array and substrate is a key parameter that affects the coupling of the localized SPhPs and propagating surface modes. We study the effect of z_0/R on the enhancement ratio Φ in the presence of different substrates. It can be seen from Fig. 7 that as z_0/R increases, Φ gradually decreases for all systems. These ten-particle systems converge to the multiparticle effect, while the two-particle system is close to a state of two isolated NPs in the free space. This suggests that the surface modes induced by substrates diminish with the increase of z_0/R until they fade away. In addition, compared to two particles in vacuum, the maximum Φ produced by ten particles in the presence of a NW goes beyond 400, which is significantly higher than that of the thin film and semi-infinite slab structures under the same conditions. For two NW systems, the interactions of localized SPhPs in the ten-particle system can provide an ultrastrong channel for energy transport, thus significantly enhancing heat exchange between the NPs at both ends. Finally, we observe that the enhancement ratio Φ in the presence of thin film is consistent with that of a semi-infinite slab for the same number of particles $N = 10$, and both have roughly similar transport properties at this distance. Interestingly, when $z_0/R = 4$, the Φ produced by two particles in the presence of a NW is close to that of the ten-particle system with a thin film or a semi-infinite slab, which indicates that the dielectric NW has excellent transport performance.

The coupling of multiparticle effects with propagating surface modes is stronger at a small distance z_0. Here, to get more insight into the coupling mechanism, we explore the spectral RHT thermal conductance $h(\omega)$ between NPs at both ends when $z_0 = 20$ nm, as shown in Fig. 8. It is seen that compared with two NPs in a vacuum, the dual waveguide mode caused by the coupling of the one-dimensional linear NP array and NW system produces a higher and wider resonance peak, which contributes to the RHT between NPs. The $h(\omega)$ of the ten-particle system with a NW is enhanced in the global range from low to high frequencies compared to the ten-particle system in vacuum. Comparably, the ten-particle system in the presence of a thin film only shows a significant increase at ω_m. Therefore, the dielectric NW can also exhibit excellent transport properties in NP array systems. Furthermore, by comparing the two NW systems, it is also found that multiparticle effects lead to a slight shift of the resonance to the left and an overall increase of the peak at ω_{np}. This may be attributed to the strong interactions of localized SPhPs in the one-dimensional linear NP array.

To visually display the dual waveguide effect arising from the linear NP array and dielectric NW, the electric field energy density $u_e(\mathbf{r}, \omega)$ for a system consisting of ten NPs and a NW is shown in Fig. 9(a). We simultaneously display the $u_e(\mathbf{r}, \omega)$ of two-particle systems in the presence of a NW and in vacuum [see Figs. 9(b) and 9(c)], respectively. It can be seen that energy can be transported from P_1 to P_2 via the coupling effect of localized SPhPs in the linear NP array. Interestingly, the energy density produced by the ten-particle system with a NW in regions far away from NPs is lower than that of the two-particle system with a NW, and even lower than that of two NPs in a vacuum. Due to the strong interactions of localized SPhPs, the high-energy density produced by P_1 is confined in the vicinity of linear arrays, thus reducing radiation into the surroundings and leading to energy being robustly transported to P_2 along the NP array. It can be considered that the multiparticle effect can not only enhance energy transport along the linear NP waveguide but also reduce radiation to the surrounding medium. Therefore, the dual

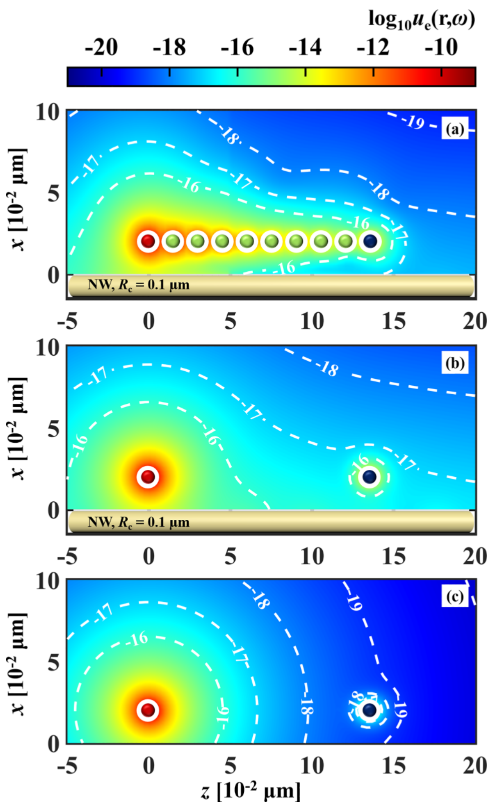

FIG. 9. The electric field energy density $u_e(\mathbf{r}, \omega)$ distribution for the cases of $\omega_{\rm np}$. (a) Ten NPs in the presence of NW, (b) two NPs with a NW, and (c) two NPs in vacuum.

waveguide mode consisting of dielectric NW and linear NP arrays can realize ultrastrong, long-distance energy transfer, which exhibits potential applications in energy management and transport at the micro- and nanoscale.

IV. CONCLUSIONS

In conclusions, we have investigated the RHT between NPs in a many-body system composed of NPs and a dielectric NW. The thermal conductance h in the presence of a NW, thin film, and semi-infinite slab is calculated, respectively. The results have shown that the NW has excellent performance for enhancing RHT between NPs as compared to planar structures, and the maximum enhancement ratio Φ can reach up to five orders of magnitude. The Φ as a function of the radius of the NW and interparticle distances is investigated, and it has been found that the Φ first increases and then decreases with the increase of R_c at a long distance d. The amplification phenomenon can be interpreted by the spectral analysis, the scattering GF, the dispersion relation, and the electric field energy density distribution. Subsequently, we have constructed a dual waveguide system composed of a dielectric NW and one-dimensional linear NP arrays. It has been validated theoretically that, due to the synergistic effect between the coupling localized SPhPs and the propagating surface modes, the dual waveguide mode can compensate for the reduction of photon-mediated RHT caused by the increase in spacing, thus achieving ultrastrong, long-range energy transport.

The present works have important application value in energy management and transport at the micro- and nanoscale. Nanowires supporting the propagating surface modes can be employed as waveguides to realize long-range electromagnetic energy transport beyond the diffraction limit. Ultracompact nanostructures exhibit outstanding performance for enhancing field confinement. The combination of the two will demonstrate robust thermal transport properties, which have potential prospects in the energy conversion and management of noncontact optoelectronic devices.

ACKNOWLEDGMENTS

This work was supported by the Key Research and Development Project of Ministry of Science and Technology (Grant No. 2022YFC2204300), the National Natural Science Foundation of China (Grants No. 52076056, No. U22A20210, and No. 52227813), and the Natural Science Foundation of Heilongjiang Province (Grant No. LH2020E046).

APPENDIX A: OUTGOING WAVES OF CYLINDRICAL HARMONICS

According to the scattering theory of electromagnetic waves, the outgoing solution of the scatter wave equation in cylindrical coordinates (r, φ, z) can be described as [60]

$$\psi_n(q, k_z, \mathbf{r}) = H_n(qr)e^{ik_z z+in\varphi}, \tag{A1}$$

where H_n is the Hankel function of the first kind. The vector cylindrical wave functions are solved by $\mathbf{M}^{\rm out}_{n,k_z}(\mathbf{r}) = \nabla \times [\psi_n(q, k_z, \mathbf{r})\mathbf{e}_z]$ and $\mathbf{N}^{\rm out}_{n,k_z}(\mathbf{r}) = \nabla \times \nabla \times [\psi_n(q, k_z, \mathbf{r})\mathbf{e}_z]/k_0$. The magnetic multipole (TE) $\mathbf{M}^{\rm out}_{n,k_z}(\mathbf{r})$ and electric multipole (TM) $\mathbf{N}^{\rm out}_{n,k_z}(\mathbf{r})$ waves in component form can be written respectively as

$$\mathbf{M}^{\rm out}_{n,k_z}(\mathbf{r}) = \left(\frac{in}{qr}H_n(qr)\mathbf{e}_r - H_n'(qr)\mathbf{e}_\varphi\right)e^{ik_z z+in\varphi}, \tag{A2}$$

$$\mathbf{N}^{\rm out}_{n,k_z}(\mathbf{r}) = \frac{1}{k_0}\left(ik_z H_n'(qr)\mathbf{e}_r - \frac{nk_z}{qr}H_n(qr)\mathbf{e}_\varphi + qH_n(qr)\mathbf{e}_z\right)e^{ik_z z+in\varphi}, \tag{A3}$$

where k_z and q are the wave vectors parallel and perpendicular to the cylinder z axis.

APPENDIX B: SCATTERING GREEN'S FUNCTION FOR PLANAR CONFIGURATIONS

The scattering Green's function for two planar configurations (semi-infinite slab and thin film) can be described in the Cartesian coordinate system (x, y, z) as [27,49]

$$\mathbb{G}_{\rm sc} = \frac{i}{8\pi^2}\int_0^{+\infty}\left[r_s\mathbf{M}^s_{\rm ref} + r_p\mathbf{M}^p_{\rm ref}\right]e^{2ik_x z_0}k_\rho dk_\rho, \tag{B1}$$

where $x = rcos\varphi$, $y = rsin\varphi$. In this work, the angle is set to $\varphi = 0$. k_x is the x component of the wave vector in a vacuum, r_s and r_p are the Fresnel reflection coefficients for two polarizations, respectively. $k_\rho = \sqrt{k_y^2 + k_z^2}$ is the wave vector component parallel to the planar surface. The matrices $\mathbf{M}^s_{\rm ref}$ and $\mathbf{M}^p_{\rm ref}$ can be written as

$$\mathbf{M}^s_{\rm ref} = \frac{2\pi}{k_x}\begin{bmatrix} \frac{1}{2}[J_0(k_\rho d_z) + J_2(k_\rho d_z)] & 0 & 0 \\ 0 & \frac{1}{2}[J_0(k_\rho d_z) - J_2(k_\rho d_z)] & 0 \\ 0 & 0 & 0 \end{bmatrix}, \tag{B2}$$

and

$$\mathbf{M}^p_{\rm ref} = \frac{2\pi}{k_0^2}\begin{bmatrix} -\frac{k_x}{2}[J_0(k_\rho d_z) - J_2(k_\rho d_z)] & 0 & -ik_\rho J_1(k_\rho d_z) \\ 0 & -\frac{k_x}{2}[J_0(k_\rho d_z) + J_2(k_\rho d_z)] & 0 \\ ik_\rho J_1(k_\rho d_z) & 0 & \frac{k_\rho^2}{k_x} J_0(k_\rho d_z) \end{bmatrix}, \tag{B3}$$

where d_z is the distance between the two NPs along the z axis and J_n is the cylindrical Bessel function of order n. When the configuration is a semi-infinite slab, the reflection coefficient at both polarizations can be expressed as

$$r_s = \frac{k_x - k_{xm}}{k_x + k_{xm}}, r_p = \frac{\varepsilon(\omega)k_x - k_{xm}}{\varepsilon(\omega)k_x + k_{xm}}, \tag{B4}$$

where $k_{xm} = \sqrt{\varepsilon(\omega)k_0^2 - k_\rho^2}$. In addition, the reflection coefficient of the thin film can be written as

$$r_s = \frac{r_s - r_s^2\, e^{2ik_{xm}\delta}}{1 - r_s^2\, e^{2ik_{xm}\delta}}, r_p = \frac{r_p - r_p^2\, e^{2ik_{xm}\delta}}{1 - r_p^2\, e^{2ik_{xm}\delta}}, \tag{B5}$$

where we can substitute Eq. (B4) into Eq. (B5) for the calculation.

[1] A. I. Volokitin and B. N. J. Persson, Near-field radiative heat transfer and noncontact friction, Rev. Mod. Phys. **79**, 1291 (2007).

[2] Z. M. Zhang, *Nano/Microscale Heat Transfer* (Springer, Cham, Switzerland, 2020).

[3] V. Fernández-Hurtado, A. I. Fernández-Domínguez, J. Feist, F. J. García-Vidal, and J. C. Cuevas, Super-Planckian far-field radiative heat transfer, Phys. Rev. B **97**, 045408 (2018).

[4] M. Nikbakht and F. Bahmani, Topological edge states in nanoparticle chains: Isolating radiative heat flux, Phys. Rev. B **108**, 064307 (2023).

[5] M. Pascale, M. Giteau, and G. T. Papadakis, Perspective on near-field radiative heat transfer, Appl. Phys. Lett. **122**, 100501 (2023).

[6] Y. Zhang, H.-L. Yi, and H.-P. Tan, Near-field radiative heat transfer between black phosphorus sheets via anisotropic surface plasmon polaritons, ACS Photonics **5**, 3739 (2018).

[7] Z. Zhang and L. Zhu, Nonreciprocal thermal photonics for energy conversion and radiative heat transfer, Phys. Rev. Appl. **18**, 027001 (2022).

[8] X. Guo, N. Li, X. Yang, R. Qi, C. Wu, R. Shi, Y. Li, Y. Huang, F. J. Garcia de Abajo, E. G. Wang, P. Gao, and Q. Dai, Hyperbolic whispering-gallery phonon polaritons in boron nitride nanotubes, Nat. Nanotechnol. **18**, 529 (2023).

[9] D.-m. Kim, S. Choi, J. Cho, M. Lim, and B. J. Lee, Boosting thermal conductivity by surface plasmon polaritons propagating along a thin Ti film, Phys. Rev. Lett. **130**, 176302 (2023).

[10] Z. Pan, G. Lu, X. Li, J. R. McBride, R. Juneja, M. Long, L. Lindsay, J. D. Caldwell, and D. Li, Remarkable heat conduction mediated by non-equilibrium phonon polaritons, Nature (London) **623**, 307 (2023).

[11] G. Jia, J. Luo, H. Wang, Q. Ma, Q. Liu, H. Dai, and R. Asgari, Two-dimensional natural hyperbolic materials: From polaritons modulation to applications, Nanoscale **14**, 17096 (2022).

[12] G. Jia, W. Xue, Z. Jia, and M. Schubert, Giant photonic spin Hall effect induced by hyperbolic shear polaritons, Phys. Chem. Chem. Phys. **25**, 11245 (2023).

[13] P. Ben-Abdallah, Multitip near-field scanning thermal microscopy, Phys. Rev. Lett. **123**, 264301 (2019).

[14] R. Mittapally, B. Lee, L. Zhu, A. Reihani, J. W. Lim, D. Fan, S. R. Forrest, P. Reddy, and E. Meyhofer, Near-field thermophotovoltaics for efficient heat to electricity conversion at high power density, Nat. Commun. **12**, 4364 (2021).

[15] Y. Hu, H. Liu, B. Yang, K. Shi, M. Antezza, X. Wu, and Y. Sun, High-rectification near-field radiative thermal diode using Weyl semimetals, Phys. Rev. Mater. **7**, 035201 (2023).

[16] Y. Li, Y. Dang, S. Zhang, X. Li, Y. Jin, P. Ben-Abdallah, J. Xu, and Y. Ma, Radiative thermal transistor, Phys. Rev. Appl. **20**, 024061 (2023).

[17] K. Joulain, J.-P. Mulet, F. Marquier, R. Carminati, and J.-J. Greffet, Surface electromagnetic waves thermally excited: Radiative heat transfer, coherence properties and Casimir forces revisited in the near field, Surf. Sci. Rep. **57**, 59 (2005).

[18] A. Narayanaswamy and G. Chen, Thermal near-field radiative transfer between two spheres, Phys. Rev. B **77**, 075125 (2008).

[19] S. J. Rahi, T. Emig, N. Graham, R. L. Jaffe, and M. Kardar, Scattering theory approach to electrodynamic Casimir forces, Phys. Rev. D **80**, 085021 (2009).

[20] L. Y. Carrillo and Y. Bayazitoglu, Nanorod near-field radiative heat exchange analysis, J. Quant. Spectrosc. Radiat. Transfer **112**, 412 (2011).

[21] M. Krüger, T. Emig, and M. Kardar, Nonequilibrium electromagnetic fluctuations: Heat transfer and interactions, Phys. Rev. Lett. **106**, 210404 (2011).
[22] A. Manjavacas and F. J. García de Abajo, Radiative heat transfer between neighboring particles, Phys. Rev. B **86**, 075466 (2012).
[23] P. Ben-Abdallah, S. A. Biehs, and K. Joulain, Many-body radiative heat transfer theory, Phys. Rev. Lett. **107**, 114301 (2011).
[24] S. A. Biehs, R. Messina, P. S. Venkataram, A. W. Rodriguez, J. C. Cuevas, and P. Ben-Abdallah, Near-field radiative heat transfer in many-body systems, Rev. Mod. Phys. **93**, 025009 (2021).
[25] P. J. Compaijen, V. A. Malyshev, and J. Knoester, Surface-mediated light transmission in metal nanoparticle chains, Phys. Rev. B **87**, 205437 (2013).
[26] J. Dong, J. Zhao, and L. Liu, Long-distance near-field energy transport via propagating surface waves, Phys. Rev. B **97**, 075422 (2018).
[27] R. Messina, S.-A. Biehs, and P. Ben-Abdallah, Surface-mode-assisted amplification of radiative heat transfer between nanoparticles, Phys. Rev. B. **97**, 165437 (2018).
[28] K. Shi, F. Bao, and S. He, Enhanced near-field thermal radiation based on multilayer graphene-hBN heterostructures, ACS Photonics **4**, 971 (2017).
[29] B. Zhao, B. Guizal, Z. M. Zhang, S. Fan, and M. Antezza, Near-field heat transfer between graphene/hBN multilayers, Phys. Rev. B **95**, 245437 (2017).
[30] J.-L. Fang, L. Qu, Y. Zhang, and H.-L. Yi, Resonant radiative heat transfer and many-body effects between nanoparticles and a multilayered slab, Phys. Rev. B **102**, 245418 (2020).
[31] J.-L. Fang, L. Qu, and H.-L. Yi, Thermal switching of near-field radiative heat transfer between nanoparticles via multilayered surface modes, Phys. Rev. Appl. **17**, 034040 (2022).
[32] Y. Zhang, J.-Y. Wang, F.-Q. Wang, Z.-M. Cai, and H.-L. Yi, Enhanced radiative heat transfer via the coupling of multi-particle interactions with combined surface models, Int. J. Heat Mass Transfer **215**, 124528 (2023).
[33] K. Asheichyk, B. Müller, and M. Krüger, Heat radiation and transfer for point particles in arbitrary geometries, Phys. Rev. B **96**, 155402 (2017).
[34] Y. Zhang, M. Antezza, H.-L. Yi, and H.-P. Tan, Metasurface-mediated anisotropic radiative heat transfer between nanoparticles, Phys. Rev. B **100**, 085426 (2019).
[35] Y. Zhang, C.-L. Zhou, H.-L. Yi, and H.-P. Tan, Radiative thermal diode mediated by nonreciprocal graphene plasmon waveguides, Phys. Rev. Appl. **13**, 034021 (2020).
[36] Y.-C. Hao, Y. Zhang, and H.-L. Yi, Near-field radiative heat transfer of nanoparticles mediated by moving metasurfaces, Phys. Rev. B **108**, 125431 (2023).
[37] E. Noruzifar, T. Emig, and R. Zandi, Universality versus material dependence of fluctuation forces between metallic wires, Phys. Rev. A **84**, 042501 (2011).
[38] V. A. Golyk, M. Kruger, and M. Kardar, Heat radiation from long cylindrical objects, Phys. Rev. E **85**, 046603 (2012).
[39] V. A. Golyk, M. Krüger, M. T. H. Reid, and M. Kardar, Casimir forces between cylinders at different temperatures, Phys. Rev. D. **85**, 065011 (2012).
[40] K. Asheichyk, P. Ben-Abdallah, M. Krüger, and R. Messina, Long-range super-Planckian heat transfer between nanoemitters in a resonant cavity, Phys. Rev. B **108**, 155401 (2023).
[41] K. Asheichyk and M. Kruger, Radiative heat transfer with a cylindrical waveguide decays logarithmically slow, Phys. Rev. Lett. **129**, 170605 (2022).
[42] P. Ben-Abdallah, R. Messina, S. A. Biehs, M. Tschikin, K. Joulain, and C. Henkel, Heat superdiffusion in plasmonic nanostructure networks, Phys. Rev. Lett. **111**, 174301 (2013).
[43] J. Dong, J. Zhao, and L. Liu, Radiative heat transfer in many-body systems: Coupled electric and magnetic dipole approach, Phys. Rev. B **95**, 125411 (2017).
[44] Y.-J. Zhang, Y. Zhang, S.-H. Yang, and H.-L. Yi, Strain-induced control of radiative heat transfer between nanoparticles in a plasmonic cavity, Int. J. Heat Mass Transfer **202**, 123677 (2023).
[45] Y. Zhang, H.-L. Yi, H.-P. Tan, and M. Antezza, Giant resonant radiative heat transfer between nanoparticles, Phys. Rev. B **100** 134305 (2019).
[46] F. Herz and S.-A. Biehs, Generalized coupled dipole method for thermal far-field radiation, Phys. Rev. B **105**, 205422 (2022).
[47] R. Messina, M. Tschikin, S.-A. Biehs, and P. Ben-Abdallah, Fluctuation-electrodynamic theory and dynamics of heat transfer in systems of multiple dipoles, Phys. Rev. B **88**, 104307 (2013).
[48] M. Krüger, G. Bimonte, T. Emig, and M. Kardar, Trace formulas for nonequilibrium Casimir interactions, heat radiation, and heat transfer for arbitrary objects, Phys. Rev. B **86**, 115423 (2012).
[49] J.-L. Fang, L. Qu, Y. Zhang, and H.-L. Yi, High enhancement of near-field radiative heat transfer between nanoparticles via the surface modes of the dielectric thin film, Int. J. Heat Mass Transfer **190**, 122711 (2022).
[50] A. W. Snyder and J. D. Love, *Optical Waveguide Theory* (Springer, New York, 1983).
[51] N. Lukas and H. Bert, *Principles of Nano-Optics* (Cambridge University Press, Cambridge, UK, 2012).
[52] Y. Gao, G. Ren, B. Zhu, H. Liu, Y. Lian, and S. Jian, Analytical model for plasmon modes in graphene-coated nanowire, Opt. Express **22**, 24322 (2014).
[53] Y. Gao, G. Ren, B. Zhu, J. Wang, and S. Jian, Single-mode graphene-coated nanowire plasmonic waveguide, Opt. Lett. **39**, 5909 (2014).
[54] L. Novotny, Effective wavelength scaling for optical antennas, Phys. Rev. Lett. **98**, 266802 (2007).
[55] J. Ordonez-Miranda, L. Tranchant, S. Gluchko, and S. Volz, Energy transport of surface phonon polaritons propagating along a chain of spheroidal nanoparticles, Phys. Rev. B **92**, 115409 (2015).
[56] B. X. Wang and C. Y. Zhao, Topological phonon polaritons in one-dimensional non-Hermitian silicon carbide nanoparticle chains, Phys. Rev. B **98**, 165435 (2018).
[57] E. Tervo, M. Francoeur, B. Cola, and Z. Zhang, Thermal radiation in systems of many dipoles, Phys. Rev. B **100**, 205422 (2019).
[58] H. Salihoglu, Z. Li, and S. Shen, Theory of thermal radiation from a nanoparticle array, Appl. Phys. Lett. **121**, 241701 (2022).
[59] T. Huang, B. Wang, W. Zhang, and C. Zhao, Ultracompact energy transfer in anapole-based metachains, Nano Lett. **21**, 6102 (2021).
[60] L. Tsang, J. A. Kong, and K.-H. Ding, *Scattering of Electromagnetic Waves: Theories and Applications* (Wiley, New York, 2000).